IOP PUBLISHING INVERSE PROBLEMS

Inverse Problems **23** (2007) 1135–1160 doi:10.1088/0266-5611/23/3/018

Effect of discretization error and adaptive mesh generation in diffuse optical absorption imaging: II

Murat Guven[1], Birsen Yazici[1], Kiwoon Kwon[1], Eldar Giladi[2] and Xavier Intes[3]

[1] Electrical, Computer, and Systems Engineering Department, Rensselaer Polytechnic Institute, Troy, NY, USA
[2] Department of Mathematical Sciences, Rensselaer Polytechnic Institute, Troy, NY, USA
[3] Department of Biomedical Engineering, Rensselaer Polytechnic Institute, Troy, NY, USA

E-mail: yazici@ecse.rpi.edu

Received 28 September 2006
Published 15 May 2007
Online at stacks.iop.org/IP/23/1135

Abstract

In part I (Guven *et al* 2007 *Inverse Problems* **23** 1115–33), we analysed the error in the reconstructed optical absorption images resulting from the discretization of the forward and inverse problems. Our analysis led to two new error estimates, which present the relationship between the optical absorption imaging accuracy and the discretization error in the solutions of the forward and inverse problems. In this work, based on the analysis presented in part I, we develop new adaptive discretization schemes for the forward and inverse problems in order to reduce the error in the reconstructed images resulting from discretization. The proposed discretization schemes lead to adaptively refined composite meshes that yield the desired level of imaging accuracy while reducing the size of the discretized forward and inverse problems. We present numerical experiments to validate the error estimates developed in part I and show the improvement in the accuracy of the reconstructed optical images with the new adaptive mesh generation algorithms.

(Some figures in this article are in colour only in the electronic version)

1. Introduction

Numerical approaches in solving the forward and inverse problems in diffuse optical tomography (DOT) pose a tradeoff between computational efficiency and imaging accuracy. This tradeoff is a direct consequence of the discretization of the forward and inverse problems [2, 9] and the size of the resulting discrete forward and inverse problems. The imaging accuracy depends on the discretization error in the forward and inverse problem solutions. On the other hand, attempting to minimize the discretization error in the solutions of both

problems separately implies a significant increase in the size of the discrete forward and inverse problems. Hence, it is important to understand the relationship between the discretization error and the resulting error in the solution of the inverse problem. Such a relationship can illuminate the mutual dependence of the forward and inverse problem solutions and identify the factors that control the extent to which the discretization error in the solutions of the forward and inverse problems affects the accuracy of the reconstructed optical images.

In part I of this two-part study, we presented an error analysis which showed the effect of discretization of the forward and inverse problems on the accuracy of the reconstructed optical absorption images [9]. The analysis led to two new error estimates that took into account the interdependence of the forward and inverse problems (see section 2). In the second part of our work, based on the error analysis presented in part I, we develop new adaptive discretization schemes for the forward and inverse problems. The resulting locally refined meshes reduce the error in the reconstructed optical images while keeping the size of the discrete forward and inverse problems relatively small.

There has been extensive research on adaptive mesh generation for the numerical solution of partial differential equations (see [9] for a list of publications) and inverse parameter estimation problems to reduce the undesired effect of discretization error [4, 14]. In the area of DOT, in [3] it was numerically shown that approximation errors resulting from the discretization of the forward problem can lead to significant degradation in the quality of the reconstructed images. In that work, the error in the reconstructed images is minimized by using an enhanced imaging model that treats this additional approximation error within the Bayesian framework. Alternatively, several investigators have reported on adaptive discretization schemes for the forward and inverse problems to address the optical image degradation due to discretization. In [6] a 'data-driven zonation' scheme, which can be viewed as an adaptive discretization algorithm, was proposed for fluorescence imaging [6]. In [8], we presented a region-of-interest (ROI) imaging scheme for DOT, which employed a multi-level algorithm on a non-uniform grid. The non-uniform grid is designed so as to provide finer spatial resolution for the ROI which corresponds to the tumour region as indicated by *a priori* anatomical image. In [16] an *a priori* non-uniform mesh design which provides high resolution at the heterogeneities and near boundary regions was proposed. In that work, the mesh refinement is independent of the source–detector configuration and the location of the heterogeneities. In [7] a dual mesh strategy was proposed, in which, a relatively fine uniform mesh is considered for the forward problem discretization and a coarse uniform mesh is generated for the inverse problem discretization. In the same study, an adaptive refinement scheme was proposed for the inverse problem discretization, but no adaptive refinement was considered for the solution of the forward problem. Another dual mesh strategy which makes use of *a priori* ultrasound information was presented in [10]. In that work, the dual mesh is a coarse mesh for the background tissue and a relatively fine mesh for the heterogeneity, similar to the approach in [8]. In fluorescence imaging, a dual adaptive mesh strategy was used to discretize the inverse problem and the associated coupled diffusion equations, where the refinement criterion is based on *a posteriori* discretization error estimates [12]. Note that in all these studies [6–8, 10, 12, 16], the mesh refinement criteria considered for the inverse (forward) problem disregard the impact of the solution of the forward (inverse) problem. In other words, the discretization of each problem is considered independently of the solution of the other problem.

In this work, based on the two error bounds provided by the error analysis in part I [9], we introduce an adaptive discretization scheme for the forward and inverse problems, respectively. We remark that the mesh refinement criterion for each problem comprises the discretization error in the corresponding problem solution, scaled spatially by the solutions of both problems.

Table 1. Definition of function spaces and norms.

Notation	Explanation
$\overline{f}$	The complex conjugate of the function f
$C(\Omega)$	Space of continuous complex-valued functions on Ω
$C^k(\Omega)$	Space of complex-valued k-times continuously differentiable functions on Ω
$L^\infty(\Omega)$	$L^\infty(\Omega) = \{f \mid \text{ess sup}_\Omega \lvert f(\mathbf{x})\rvert < \infty\}$
$L^p(\Omega)$	$L^p(\Omega) = \left\{ f \,\middle|\, \left(\int_\Omega \lvert f(\mathbf{x})\rvert^p \, d\mathbf{x} \right)^{1/p} < \infty \right\}$, $p \in [1, \infty(b))$
$D_w^z f$	zth weak derivative of f
$H^p(\Omega)$	$H^p(\Omega) = \left\{ f \,\middle|\, \left(\sum_{\lvert z\rvert \leqslant p} \left\lVert D_w^z f \right\rVert_0^2 \right)^{1/2} < \infty \right\}$, $p \in [1, \infty)$
$\lVert f\rVert_0$	The $L^2(\Omega)$ norm of f
$\lVert f\rVert_p$	The $H^p(\Omega)$ norm of f
$\lVert f\rVert_\infty$	The $L^\infty(\Omega)$ norm of f
$\lVert f\rVert_{L^p(\Omega)}$	The $L^p(\Omega)$ norm of f
$\lVert f\rVert_{0,m}$	The L^2 norm of f over the mth finite element Ω_m
$\lVert f\rVert_{p,m}$	The H^p norm of f over the mth finite element Ω_m

Thus, the proposed adaptive mesh generation algorithms address the interdependence between the solutions of the forward and inverse problems and take into account the orientation of the source–detectors and the absorptive perturbations. This makes the adaptive discretization algorithms introduced in this paper different from the previous approaches [6–8, 10, 12, 16]. The simulation experiments validate the implications of our error analysis and show that the proposed mesh generation algorithms significantly improve the accuracy of the reconstructed optical images for a given number of unknowns in the discrete forward and inverse problems. We specifically show that using the discretization error estimates, which do not take into account the interdependence of forward and inverse problems as a criterion for discretization, may lead to severely degraded image reconstructions (see simulation study 3). We also discuss the computational complexity of the proposed adaptive mesh generation algorithms and compare it to the computational complexity of mesh generation algorithms based on the conventional discretization error estimates. We finally note that the proposed adaptive mesh generation algorithms can be adapted for similar inverse parameter estimation problems, such as electrical impedance tomography, optical fluorescence tomography, bioluminescence tomography, microwave imaging, etc.

The outline of this paper is as follows: in section 2, we give a brief overview of the forward and inverse DOT problems and recall the two theorems presented in part I which summarize the impact of discretization on the accuracy of the reconstructed optical images. In section 3, based on these two theorems, we introduce the adaptive mesh generation algorithms for the solution of the forward and inverse problems and discuss their computational complexity. In section 4, we present our experimental results, which is followed by section 5. The appendix includes the solution of a model problem used to initiate the adaptive mesh generation.

2. Overview

In this section, we first briefly define the forward and inverse problems in DOT. Next, we state theorems 1 and 2 presented in the first part of this work [9] to recall the effect of the discretization of the forward and inverse problems on the accuracy of optical absorption image reconstruction. We refer to table 1 for the explanation of the notation associated with functions

and their norms. Note that calligraphic letters are used to denote the operators, e.g. $\mathcal{A}_a, \mathcal{I}$, $\mathcal{K}$ etc.

2.1. Forward and inverse problems in DOT

We consider the following boundary value problem to model the near-infrared light propagation in a bounded domain $\Omega \subset \mathbb{R}^3$ with Lipschitz boundary $\partial\Omega$ [2, 5]:

$$-\nabla \cdot D(\mathbf{x})\nabla g_j(\mathbf{x}) + \left(\mu_a(\mathbf{x}) + \frac{\mathrm{i}\omega}{c}\right) g_j(\mathbf{x}) = Q_j(\mathbf{x}) \qquad \mathbf{x} \in \Omega, \tag{2.1}$$

$$g_j(\mathbf{x}) + 2aD(\mathbf{x})\frac{\partial g_j}{\partial n}(\mathbf{x}) = 0 \qquad \mathbf{x} \in \partial\Omega, \tag{2.2}$$

where $g_j(\mathbf{x})$ is the photon density at $\mathbf{x}$, Q_j is the point source located at the source position $\mathbf{x}_s^j$, $j = 1, \ldots, N_s$, where N_s is the number of sources, $D(\mathbf{x})$ is the diffusion coefficient and $\mu_a(\mathbf{x})$ is the absorption coefficient at $\mathbf{x}$, $\mathrm{i} = \sqrt{-1}$, ω is the modulation frequency of the source, c is the speed of the light, $a = (1 + R)/(1 - R)$ where R is a parameter governing the internal reflection at the boundary $\partial\Omega$, and $\partial \cdot /\partial n$ denotes the directional derivative along the unit normal vector on the boundary. The boundary value problem (2.1)–(2.2) constitutes the forward problem in DOT together with the associated adjoint problem [2, 9]:

$$-\nabla \cdot D(\mathbf{x})\nabla g_i^*(\mathbf{x}) + \left(\mu_a(\mathbf{x}) - \frac{\mathrm{i}\omega}{c}\right) g_i^*(\mathbf{x}) = 0 \qquad \mathbf{x} \in \Omega, \tag{2.3}$$

$$g_i^*(\mathbf{x}) + 2aD(\mathbf{x})\frac{\partial g_i^*}{\partial n}(\mathbf{x}) = Q_i^*(\mathbf{x}) \qquad \mathbf{x} \in \partial\Omega, \tag{2.4}$$

where Q_i^* is the adjoint source located at the detector position $\mathbf{x}_d^i$, $i = 1, \ldots, N_d$, where N_d is the number of detectors. Note that we approximate the point source Q_j in (2.1) and the adjoint source Q_i^* in (2.4) by Gaussian functions with sufficiently low variance, whose centres are located at $\mathbf{x}_s^j$ and $\mathbf{x}_d^i$, respectively.

In this work, we focus on the estimation of the absorption coefficient and consider an iterative algorithm based on repetitive linearization of the inverse problem using first-order Born approximation. Using a zeroth-order Tikhonov regularization to address the illposedness, the inverse problem at each iteration reads

$$\begin{aligned}\gamma(\mathbf{x}) &:= (\mathcal{A}_a^*\Gamma)(\mathbf{x}) = [(\mathcal{A}_a^*\mathcal{A}_a + \lambda\mathcal{I})\alpha^\lambda](\mathbf{x}) \\ &:= \int_\Omega \kappa(\mathbf{x}, \acute{\mathbf{x}})\alpha^\lambda(\acute{\mathbf{x}})\,\mathrm{d}\acute{\mathbf{x}} + \lambda\alpha^\lambda(\mathbf{x}) \qquad (2.5) \\ &:= (\mathcal{K}\alpha^\lambda)(\mathbf{x}), \qquad (2.6)\end{aligned}$$

where $\Gamma \in \mathbb{C}^{N_d \times N_s}$ is the vector of differential measurements at N_d number of detectors due to N_s number of sources, as a result of the small perturbation α on the background absorption coefficient μ_a, and α^λ is the solution of the regularized inverse problem. In (2.5), $\kappa(\mathbf{x}, \acute{\mathbf{x}})$ is the kernel of the integral equation, given by [9]

$$\kappa(\mathbf{x}, \acute{\mathbf{x}}) = \sum_{i,j}^{N_d, N_s} H_{i,j}^*(\mathbf{x}) H_{i,j}(\acute{\mathbf{x}}), \tag{2.7}$$

where $H_{i,j} := -\overline{g_i^*} g_j$ is the (i, j)th kernel of the matrix-valued operator $\mathcal{A}_a : L^\infty(\Omega) \to \mathbb{C}^{N_d \times N_s}$ and $H^*_{i,j} := -g_i^* \overline{g_j}$ is the (i, j)th kernel of the adjoint operator $\mathcal{A}_a^* : \mathbb{C}^{N_d \times N_s} \to L^1(\Omega)$ defined by

$$(\mathcal{A}_a^* \beta)(\mathbf{x}) = \sum_{i,j}^{N_d, N_s} H^*_{i,j}(\mathbf{x}) \beta_{i,j} = \sum_{i,j}^{N_d, N_s} -g_i^*(\mathbf{x}) \overline{g_j(\mathbf{x})} \beta_{i,j}, \tag{2.8}$$

for all $\beta \in \mathbb{C}^{N_d \times N_s}$. We note that g_j and g_i^* in (2.7) and (2.8) are the solutions of the variational formulations of (2.1)–(2.2) and (2.3)–(2.4), respectively [9]. Assume that $D, \mu_a \in C^1(\Omega)$. Noting $Q_j, Q_i^* \in H^1(\Omega)$, the solutions $g_j, g_i^* \in H^1(\Omega)$ of the variational formulations of the boundary value problems (2.1)–(2.2) and (2.3)–(2.4) also satisfy [9]

$$g_j, g_i^* \in C(\Omega). \tag{2.9}$$

For the rest of the paper, we will denote $L^\infty(\Omega)$ and $L^1(\Omega)$ by X and Y, respectively.

Below we summarize the two theorems of part I [9] and provide the error estimates which will be used in the design of adaptive meshes for the discretization of the forward and inverse DOT problems. In this respect, we first consider the impact of the inverse problem discretization when the associated kernel $\kappa(\mathbf{x}, \hat{\mathbf{x}})$ in (2.5) is exact. Next, we give the error estimate for the case in which the kernel is replaced by its finite-dimensional approximation (i.e. degenerate kernel) and analyse the effect of the forward problem discretization on the accuracy of the reconstructed image without projecting (2.6).

2.2. *Effect of inverse problem discretization*

Let $X_n \subset X$ and $Y_n \subset Y$ denote a sequence of finite dimensional subspaces of dimension $n = 1, 2, \ldots$, spanned by first-order Lagrange basis functions $\{L_1, \ldots, L_n\}$, and $\{\mathbf{x}_p\}$, $p = 1, \ldots, n$, be the set of collocation points on Ω. Then, the discretization of the inverse problem (2.6) by projecting it onto the finite dimensional subspace Y_n using the collocation method approximates the solution of (2.6) by an element $\alpha_n^\lambda \in X_n$ which satisfies

$$\left(\mathcal{K}\alpha_n^\lambda\right)(\mathbf{x}_p) = \gamma(\mathbf{x}_p), \qquad p = 1, \ldots, n, \tag{2.10}$$

where we express $\alpha_n^\lambda(\mathbf{x})$, $\mathbf{x} \in \Omega$ on a set $\{\Omega_m\}$ of finite elements for $m = 1, \ldots, N_\Delta$ such that $\bigcup_m^{N_\Delta} \Omega_m = \Omega$ as follows:

$$\alpha_n^\lambda(\mathbf{x}) = \sum_{k=1}^{n} a_k L_k(\mathbf{x}). \tag{2.11}$$

Equivalently, the collocation method can be interpreted as a projection with the interpolation operator $\mathcal{P}_n : Y \to Y_n$ defined by [13]

$$\mathcal{P}_n f(\mathbf{x}) := \sum_{p=1}^{n} f(\mathbf{x}_p) L_p(\mathbf{x}), \qquad \mathbf{x} \in \Omega, \tag{2.12}$$

for all $f \in Y$. Then, (2.10) is equivalent to

$$\mathcal{P}_n \mathcal{K} \alpha_n^\lambda = \mathcal{P}_n \gamma. \tag{2.13}$$

Let ψ be the interpolant of α^λ [5] and assume that $\alpha^\lambda \in H^1(\Omega)$. Then, the interpolation error $e_\alpha = \alpha^\lambda - \psi$ on each finite element Ω_m is bounded by

$$\|e_\alpha\|_{0,m} \leqslant C \|\alpha^\lambda\|_{1,m} h_m, \tag{2.14}$$

where C is a positive constant and h_m is the diameter of the smallest ball that contains the mth element Ω_m.

Theorem 1 describes the effect of inverse problem discretization on the accuracy of the reconstructed optical absorption image.

Theorem 1. *Let g_j, g_i^* be the solutions of the variational formulations of the boundary value problems (2.1)–(2.2) and (2.3)–(2.4), respectively. The error between the solution α^λ of (2.6) and the solution α_n^λ of (2.13) is bounded by*

$$\left\|\alpha^\lambda - \alpha_n^\lambda\right\|_{L^1(\Omega)} \leqslant C\sqrt{V_\Omega}\|\mathcal{I} - \mathcal{T}_n\|_{Y\to X_n} \sum_{m=1}^{N_\Delta} \|\alpha^\lambda\|_{1,m} h_m + \frac{C}{\lambda}\|\mathcal{T}_n\|_{Y\to X_n} \max_{i,j} \|g_i^* g_j\|_{L^1(\Omega)} \sum_{m=1}^{N_\Delta} \sum_{i,j}^{N_d,N_s} \|g_i^* g_j\|_{0,m} \|\alpha^\lambda\|_{1,m} h_m, \tag{2.15}$$

where C is a positive constant, V_Ω is the volume of Ω, $\mathcal{T}_n : Y \to X_n$ is a uniformly bounded operator given by $\mathcal{T}_n = \left(\mathcal{I} + \frac{1}{\lambda}\mathcal{P}_n\mathcal{A}_a^*\mathcal{A}_a\right)^{-1}\mathcal{P}_n$ [9].

Proof. See [9]. □

2.3. Effect of forward problem discretization

Let $\left\{\Omega_m^j\right\}$ denote the set of linear elements used to discretize the variational formulation of the boundary value problem (2.1)–(2.2) for $m = 1, \ldots, N_\Delta^j$; such that $\bigcup_m^{N_\Delta^j} \Omega_m^j = \Omega$, and h_m^j be the diameter of the smallest ball that contains the element Ω_m^j in the finite-dimensional solution G_j, for all $j = 1, \ldots, N_s$ [9]. Similarly, let $\left\{\Omega_n^i\right\}$ denote the set of linear elements used to discretize the variational formulation of the boundary value problem (2.3)–(2.4) for $n = 1, \ldots, N_\Delta^{*i}$; such that $\bigcup_n^{N_\Delta^{*i}} \Omega_n^i = \Omega$, and h_n^i be the diameter of the smallest ball that contains the element Ω_n^i in the finite-dimensional solution G_i^*, for all $i = 1, \ldots, N_d$ [9]. Then, a bound for the discretization error in the finite element solutions G_j and G_i^* with respect to the solutions g_j and g_i^* of the variational formulations of the boundary value problems (2.1)–(2.2) and (2.3)–(2.4) on each finite element can be given by [5]

$$\|g_j - G_j\|_{0,m^j} \leqslant C\|g_j\|_{1,m^j} h_m^j, \tag{2.16}$$

$$\|g_i^* - G_i^*\|_{0,n^i} \leqslant C\|g_i^*\|_{1,n^i} h_n^i, \tag{2.17}$$

where C is a positive constant, and $\|\cdot\|_{0,m^j}$ ($\|\cdot\|_{0,n^i}$) and $\|\cdot\|_{1,m^j}$ ($\|\cdot\|_{1,n^i}$) are respectively the L^2 and H^1 norms on $\Omega_m^j\left(\Omega_n^i\right)$.

Consider the inverse problem

$$\tilde{\mathcal{K}}\tilde{\alpha}^\lambda = \tilde{\gamma}, \tag{2.18}$$

where $\tilde{\mathcal{K}}$ and $\tilde{\gamma}$ are the finite dimensional approximations to $\mathcal{K}$ and γ, obtained by substituting g_j and g_i^* in $H_{i,j}$ and $H_{i,j}^*$ by G_j and G_i^*, respectively.

Theorem 2 shows the effect of forward problem discretization on the accuracy of the reconstructed optical absorption image.

Theorem 2. *A bound for the error between the solution α^λ of (2.6) and the solution $\tilde{\alpha}^\lambda$ of (2.18) due to approximations $\tilde{\mathcal{K}}$ and $\tilde{\gamma}$ is given by*

$$\|\alpha^\lambda - \tilde{\alpha}^\lambda\|_{L^1(\Omega)} \leqslant \frac{C}{\lambda} \max_{i,j} \|g_i^* g_j\|_{L^1(\Omega)} \left(\sum_{i=1}^{N_d} \sum_{n,j}^{N_\Delta^{*i}, N_s} (2\|g_j \alpha^\lambda\|_{0,n^i} + \|\alpha\|_\infty \|g_j\|_{0,n^i}) \|g_i^*\|_{1,n^i} h_n^i \right.$$
$$\left. + \sum_{j=1}^{N_s} \sum_{m,i}^{N_\Delta^j, N_d} (2\|g_i^* \alpha^\lambda\|_{0,m^j} + \|\alpha\|_\infty \|g_i^*\|_{0,m^j}) \|g_j\|_{1,m^j} h_m^j \right), \tag{2.19}$$

where C is a positive constant.

Proof. See [9]. □

We refer to part I [9] for further details of the discussion regarding the definition and discretization of the forward and inverse problems. In the following, we discuss the adaptive mesh generation for the forward and inverse problems.

3. Adaptive mesh generation

In this section, we discuss the adaptive mesh design for the discretization of the forward and inverse problems based on theorems 1 and 2. For each problem, we present an adaptive mesh generation algorithm, which is followed by the corresponding computational cost analysis.

3.1. Adaptive mesh generation for the forward problem

Let the mesh parameter h_m^j for G_j, $j = 1, \ldots, N_s$, and the mesh parameter h_n^i for G_i^*, $i = 1, \ldots, N_d$ be chosen so that

$$h_m^j \leqslant \frac{\epsilon_f}{\sum_{i=1}^{N_d} (2\|g_i^* \alpha^\lambda\|_{0,m^j} + \|\alpha\|_\infty \|g_i^*\|_{0,m^j}) \|g_j\|_{1,m^j}} := B_j^m, \tag{3.20}$$

$$h_n^i \leqslant \frac{\epsilon_f}{\sum_{j=1}^{N_s} (2\|g_j \alpha^\lambda\|_{0,n^i} + \|\alpha\|_\infty \|g_j\|_{0,n^i}) \|g_i^*\|_{1,n^i}} := B_i^{*n}, \tag{3.21}$$

where the tolerance ϵ_f will be defined later. Then, by theorem 2, the error in the reconstructed image due to the forward problem discretization is bounded by

$$\frac{C}{\lambda} \max_{i,j} \|g_i^* g_j\|_{L^1(\Omega)} \left(\sum_{j=1}^{N_s} N_\Delta^j + \sum_{i=1}^{N_d} N_\Delta^{*i} \right) \epsilon_f = \tilde{\epsilon}^f, \tag{3.22}$$

where C is a positive constant and $\tilde{\epsilon}^f$ is the total allowable error in the reconstructed optical image due to the forward problem discretization. Equation (3.22) implies the following value for ϵ_f:

$$\epsilon_f = \frac{\lambda \tilde{\epsilon}^f / C}{\max_{i,j} \|g_i^* g_j\|_{L^1(\Omega)}} \frac{1}{\left(\sum_{j=1}^{N_s} N_\Delta^j + \sum_{i=1}^{N_d} N_\Delta^{*i} \right)}. \tag{3.23}$$

Algorithm 1 outlines the adaptive mesh generation algorithm for the forward problem in the form of a pseudocode. The algorithm is performed for each source and detector before the linearization of the inverse problem and it yields a family of adaptively refined meshes with conforming elements. We use Rivara's algorithm [15] for refinement.

Algorithm 1. The pseudocode for the mesh generation algorithm for the forward problem, prior to the linearization of the inverse problem.

◇ Generate an initial uniform mesh (Δ, N_Δ), $\Delta = \bigcup_{e=1}^{N_\Delta}\{\Delta_e\}$
◇ Set ϵ^f
◇ Initialize the set of marked elements: $M_e \leftarrow \{\}$
◇ *flag* = *True*
while flag = True
for each element $\Delta_e \in \Delta$with mesh parameter h_e^j $\left(h_e^i\right)$
if first linearization
. Use analytical solutions for g_j and g_i^* and *a priori* anatomical information about α to compute the bound B_j^m in (3.20) (B_i^{*n} in (3.21))
else
. Use current solution updates G_j and G_i^* and $\tilde{\alpha}_n^\lambda$ to compute B_j^m in (3.20) (B_i^{*n} in (3.21))
end
if $h_e^j > B_j^m$ $\left(h_e^i > B_i^{*n}\right)$
. $M_e \leftarrow M_e \bigcup\{\Delta_e\}$
end
end
if $M_e \neq \{\}$
. Refine the marked elements and update the mesh Δ
. $M_e \leftarrow \{\}$
else
. flag = False
end
end
◇ Solve for G_j (G_i^*).

Remark 1.

(i) In practice, B_j^m and B_i^{*n} in (3.20)–(3.21) cannot be computed since α, α^λ, g_j and g_i^* are unknown. However, B_j^m and B_i^{*n} can be estimated by using approximations for the functions involved in these bounds, based on either *a priori* information or on the recent forward and inverse problem solution updates. Then, the elements whose mesh parameter h_m^j $\left(h_n^i\right)$ exceeds B_j^m $\left(B_i^{*n}\right)$ can be determined and refined.

(ii) After the first sweep of refinement, one can compute the bound B_j^m and B_i^{*n} only for the new elements. We note that for the initial mesh design, we use a model problem to compute the terms in the error bound relevant to the forward problem solution (see appendix). If there is no *a priori* information, α^λ can be assumed to be spatially constant at the first linearization step. After the first linearization, the norms in B_j^m and B_i^{*n} relevant to g_j and g_i^* are not expected to change significantly. In this context, the terms $\|g_i^*\alpha^\lambda\|_{0,m^j}$, $\|g_j\alpha^\lambda\|_{0,n^i}$ in (3.20) and (3.21) can be bounded by $\|g_i^*\|_{0,m^j}\|\alpha^\lambda\|_{\infty,m^j}$ and $\|g_j\|_{0,n^i}\|\alpha^\lambda\|_{\infty,n^i}$, respectively. Therefore, one can store the norms $\|g_j\|_{0,n^i}$ and $\|g_i^*\|_{0,m^j}$ at the end of the first mesh generation, and update B_j^m and B_i^{*n} in the following mesh generations by using these stored values and the updated α^λ values.

(iii) In case ϵ_f cannot be chosen in prior, we consider a posterior approach, set $\epsilon_f = 1$, and compute $h_m^j / B_j^m \left(h_n^i / B_i^{*n}\right)$ on each element, which is used as the indicator for refinement. Then, the elements with indicator value exceeding the average $h_m^j / B_j^m \left(h_n^i / B_i^{*n}\right)$ quantity are marked for refinement. We note that in this case, the algorithm has to be stopped when the number of nodes in the mesh exceeds the allowable number of nodes.

3.2. Computational cost of the adaptive mesh generation algorithm for the forward problem

Consider the algorithm described in remark 1(iii) for $\Omega \subset \mathbb{R}^2$. Using triangular finite elements with first-order Lagrange basis functions and an analytical (exact) integration on each finite element, the number of multiplications required to compute the L^2 or H^1 norm of a finite-dimensional function on each triangular element $\Omega_m^j \left(\Omega_n^i\right)$ is 12. On the other hand, computing the norm $\|g_j \alpha^\lambda\|_{0,n^i}$ $(\|g_i^* \alpha^\lambda\|_{0,m^j})$ takes ten times the number of multiplications to compute $\|g_j\|_{1,m^j}$ $(\|g_i^*\|_{1,n^i})$. As a result, the total number of multiplications required to compute the error estimates on all finite elements for the jth source is given by $(132N_d + 16)N_\Delta^j$. Similarly, the total number of multiplications required to compute the error estimates on all finite elements for the ith detector is equal to $(132N_s + 16)N_\Delta^{*i}$.

In order to reduce the computational cost of the proposed adaptive mesh generation algorithm, we can approximate the bounds B_j^m in (3.20) and B_i^{*n} in (3.21) as follows:

$$B_j^m \approx \frac{1}{\left(2\left\|\sum_{i=1}^{N_d} g_i^* \alpha^\lambda\right\|_{0,m^j} + \|\alpha\|_\infty \left\|\sum_{i=1}^{N_d} g_i^*\right\|_{0,m^j}\right)\|g_j\|_{1,m^j}} \tag{3.24}$$

$$B_i^{*n} \approx \frac{1}{\left(2\left\|\sum_{j=1}^{N_s} g_j \alpha^\lambda\right\|_{0,n^i} + \|\alpha\|_\infty \left\|\sum_{j=1}^{N_s} g_j\right\|_{0,n^i}\right)\|g_i^*\|_{1,n^i}}. \tag{3.25}$$

Then, the number of multiplications required to compute the error estimates on all finite elements becomes $148N_\Delta^j \left(148N_\Delta^{*i}\right)$, which implies a significant reduction as compared to $(132N_d + 16)N_\Delta^j \left((132N_s + 16)N_\Delta^{i*}\right)$.

If one uses the discretization error estimates (2.16)–(2.17) to generate adaptive meshes for the discretization of (2.1)–(2.2) and (2.3)–(2.4), the number of multiplications is equal to $13N_\Delta^j$ and $13N_\Delta^{*i}$, respectively. Then, the resulting adaptive meshes will lead to finite element solutions G_j and G_i^* with reduced discretization error. However, reduction in the discretization error in G_j and G_i^* may not ensure the accuracy of the reconstructed absorption image (see simulation experiment 3).

3.3. Adaptive mesh generation for the inverse problem:

Let the mesh parameter h_m for the solution of the inverse problem be defined as follows:

$$h_m \leqslant \epsilon_{\text{inv}} \Bigg/ \Bigg(\sqrt{V_\Omega} \|\mathcal{I} - \mathcal{T}_n\|_{Y \to X_n} \|\alpha^\lambda\|_{1,m} + \frac{1}{\lambda} \|\mathcal{T}_n\|_{Y \to X_n} \times \max_{i,j} \|g_i^* g_j\|_{L^1(\Omega)} \sum_{i,j}^{N_d, N_s} \|g_i^* g_j\|_{0,m} \|\alpha^\lambda\|_{1,m} \Bigg) := B_{\text{inv}}^m. \tag{3.26}$$

Then, by theorem 1, the error in the reconstructed image due to inverse problem discretization is bounded by

$$C N_\Delta \epsilon_{\text{inv}} = \tilde{\epsilon}^{\text{inv}}, \tag{3.27}$$

where C is a positive constant and $\bar{\epsilon}^{\text{inv}}$ is the total allowable error in the reconstructed optical image due to inverse problem discretization.

We present the pseudocode for our adaptive mesh generation algorithm used at each linearization of the inverse problem in algorithm 2. Similar to the forward problem discretization, we use Rivara's algorithm [15] for the refinement of the elements.

Algorithm 2. The pseudocode for the mesh generation algorithm at every linearization step of the inverse problem.

◇ Generate an initial uniform mesh (Δ, N_Δ), $\Delta = \bigcup_{m=1}^{N_\Delta}\{\Delta_m\}$
◇ Set ϵ_{inv}
◇ Initialize the set of marked elements: $M_e \leftarrow \{\}$
◇ *flag* = *True*
while flag = True
for each element $\Delta_m \in \Delta$ with mesh parameter h_m
if first linearization
. Use current solution updates G_j and G_i^* and *a priori* information about α to compute B_{inv}^m in (3.26)
else
. Use current solution updates G_j and G_i^* and $\tilde{\alpha}_n^\lambda$ to compute B_{inv}^m in (3.26)
end
if $h_m > B_{\text{inv}}^m$
. $M_e \leftarrow M_e \bigcup\{\Delta_m\}$
end
end
if $M_e \neq \{\}$
. Refine the marked elementsand update themesh Δ
. $M_e \leftarrow \{\}$
else
. flag = False
end
end
◇ Solve for $\tilde{\alpha}_n^\lambda$.

Remark 2.

(i) In practice, B_{inv}^m in (3.26) cannot be computed since α^λ, g_j, g_i^* and $\mathcal{T}_n$ are unknown. Similar to the approach described in section 3.1, we can compute an estimate for B_{inv}^m by using the uniform boundedness of the operator $\mathcal{T}_n$ [9] and by using approximate values for the functions involved in B_{inv}^m. In this context, we use either *a priori* information or the recent forward and inverse problem solution updates to calculate (3.26) on each element. Then, the elements with the mesh parameter $h_m > B_{\text{inv}}^m$ are determined and refined.

(ii) In order to save computations, after the first sweep of refinement, one can compute the bound B_{inv}^m only for the new elements. Furthermore, similar to the approach described in section 3.1, the term $\|g_i^* g_j\|_{0,m}$ in (3.26) can be stored after the first mesh generation and can be used in the following mesh generations. In this context, the bound B_{inv}^m can be updated by using only the updated $\|\alpha^\lambda\|_{1,m}$ value.

(iii) Note that, in practice, one of the two terms in the denominator of B^m_{inv} will be dominant depending on the value of λ. Thus, we consider only the dominant term for the computation of B^m_{inv}. In case ϵ_{inv} cannot be chosen in prior, we consider a posterior approach, set $\epsilon_{\text{inv}} = 1$ and compute $\|\alpha^\lambda\|_{1,m} h_m$ or $\sum_{i,j}^{N_d,N_s} \|g_i^* g_j\|_{0,m} \|\alpha^\lambda\|_{1,m} h_m$ on each element, which are used as the refinement indicators. Then, the elements with indicator value which exceeds the average indicator value are refined. In this case, the algorithm has to be stopped when the number of nodes in the mesh exceeds the allowable number of nodes.

3.4. Computational cost of the adaptive mesh generation algorithm for the inverse problem

Consider the algorithm stated in remark 2(iii) for $\Omega \subset \mathbb{R}^2$ and assume that the second term in the denominator of B^m_{inv} (3.26) is dominant. Using triangular finite elements with first-order Lagrange basis functions and an analytical (exact) integration on each finite element, the total number of multiplications required to compute the error estimates on all finite elements is given by $(120 N_d N_s + 14) N_\Delta$.

In order to reduce the number of multiplications, we can consider an approximation for B^m_{inv} as follows:

$$B^m_{\text{inv}} \approx \frac{1}{\left\| \sum_{i,j}^{N_d,N_s} g_i^* g_j \right\|_{0,m} \|\alpha^\lambda\|_{1,m}}. \tag{3.28}$$

Then, the number of multiplications reduces to $134 N_\Delta$.

If one uses the interpolation error estimate (2.14) to generate adaptive meshes, the number of multiplications to compute the error estimates on all finite elements will be $13 N_\Delta$. However, such adaptive meshes may not help reduce the error in the reconstructed optical images, resulting from discretization (see simulation experiment 3).

4. Numerical experiments

We conduct a series of numerical experiments to demonstrate the implications of theorems 1 and 2, and to present the effectiveness of the proposed adaptive mesh generation algorithms. We perform our experiments in 2D for ease of comparison.

In the first simulation, we consider a series of image reconstructions to show the effectiveness of the proposed adaptive mesh generation algorithms. In this context, we compare the images reconstructed by using uniform meshes for the forward and inverse problems to the images reconstructed by using adaptive meshes which are designed based on theorems 1 and 2.

In the second simulation, we show the effect of the heterogeneity size on the accuracy of the reconstructed absorption images. Next, we demonstrate how this error can be addressed by the proposed adaptive discretization schemes.

In the final simulation study, we demonstrate the implication of theorem 2 and show that meshes generated for the forward problem by using discretization error estimates which disregard the interaction between the solutions g_j, g_i^* and α^λ can lead to unstable image reconstructions. We note that the proposed adaptive mesh generation algorithm for the forward problem addresses this problem.

Note that in all experiments, we use triangular finite elements with first-order Lagrange basis functions. We apply Gaussian elimination method to solve the discrete forward problem resulting from the variational formulation [5] of the boundary value problems (2.1)–(2.2)

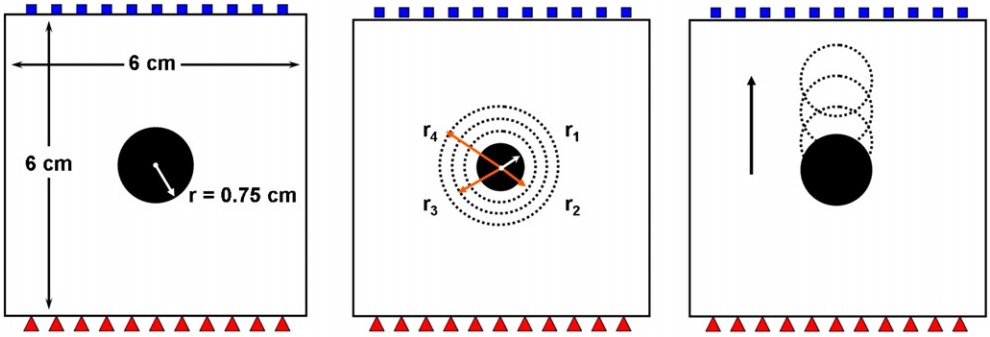

Figure 1. The setups used for the simulation studies 1, 2 and 3. The squares and triangles denote the detectors and sources, respectively. (a) The optical domain and source–detector configuration for simulation study 1. (b) The optical domain and source–detector configuration for simulation study 2. $r_1 = 0.50$ cm, $r_2 = 0.75$ cm, $r_3 = 1.0$ cm and $r_4 = 1.25$ cm. (c) The optical domain and source–detector configuration for simulation study 3. The radius of the circles is 0.75 cm.

and (2.3)–(2.4) [9]. For the inverse problem, we consider the discrete problem obtained by projecting (2.18) by the collocation method [9]:

$$\mathcal{P}_n \tilde{\mathcal{K}} \tilde{\alpha}_n^{\lambda} = \mathcal{P}_n \tilde{\gamma}, \tag{4.29}$$

where the regularization parameter is chosen as small as possible, yet large enough to enable robust image reconstructions. In this respect, an appropriate value for the regularization parameter is chosen based on experience. The discrete inverse problem (4.29) is solved using Gaussian elimination as well.

4.1. Simulation study 1

In this simulation study, we consider the geometry shown in figure 1(a). We simulate the optical data by solving the diffusion equation at $\omega = 0$ on a fine uniform grid with 81 nodes along the x and y directions, where the refractive index mismatch parameter $a = 3.11$ sources and 11 detectors are evenly spaced on the bottom and top edges of the square, respectively. The diffusion coefficient $D(\mathbf{x}) = 0.0410$ for $\mathbf{x} \in \Omega \cup \partial\Omega$. The circular heterogeneity with absorption coefficient $\mu_a = 0.2$ cm^{-1} is embedded in an optically homogeneous background with $\mu_a = 0.04$ cm^{-1}.

In order to obtain a series of absorption imaging problems using the same setup, we consider five values for the background absorption value. Then, for each imaging problem, we consider three mesh scenarios: uniform mesh for both forward and inverse problems; adaptive mesh for the forward problem and uniform mesh for the inverse problem; and adaptive meshes for both forward and inverse problems. We refer to table 2 for a brief outline of the first simulation study.

The uniform mesh used for the forward problem discretization has 625 nodes and is shown in figure 2(a). The uniform mesh for the inverse problem has 313 nodes and is shown in figure 2(b). We use the algorithms described in section 3.1 and remark 1(iii), and section 3.3 remark 2(iii) to generate the adaptive meshes for the forward and inverse problems, respectively. The number of nodes in each of the adaptive meshes used for the forward problem does not exceed 750. An example for the adaptive mesh generated for a source located at (1.0, 0) is shown in figure 2(c). The adaptive mesh for the inverse problem generated for the case where the background $\mu_a = 0.050$ cm^{-1} has 418 nodes and is shown in figure 2(d).

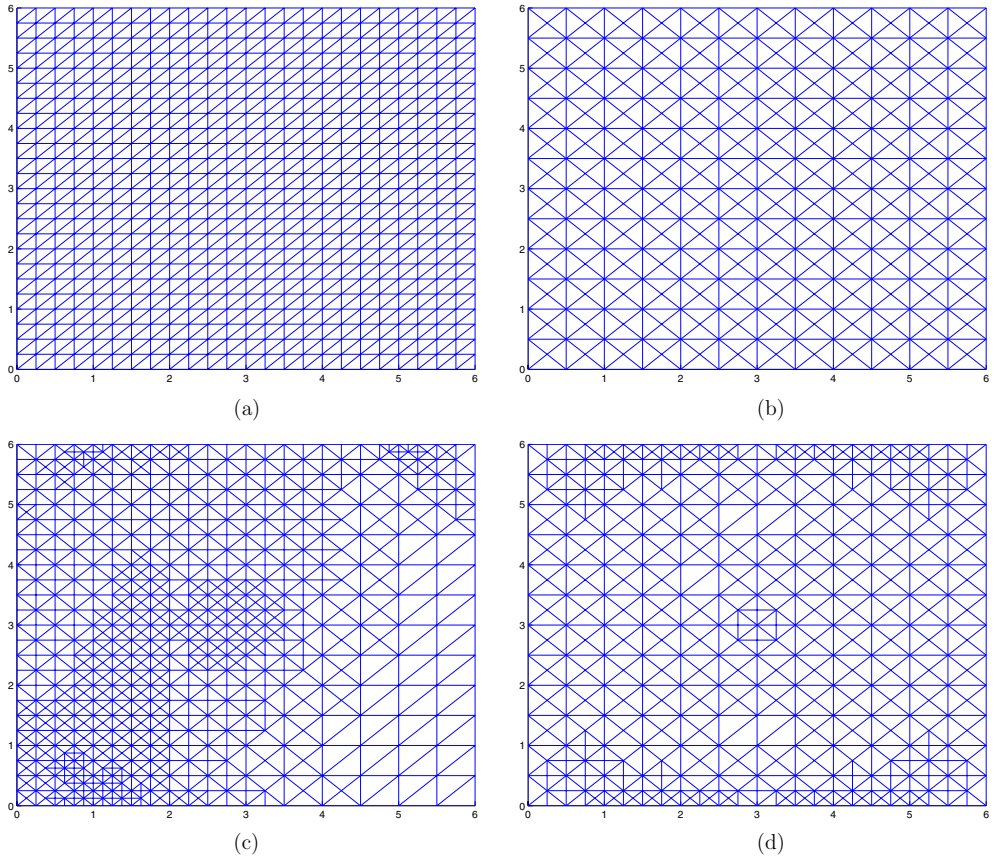

Figure 2. Examples of meshes used in the first simulation study. (a) The uniform mesh with 625 nodes. (b) The uniform mesh with 313 nodes. (c) The adaptive mesh generated for the forward problem for the source located at (1.0,0): background $\mu_a = 0.050\ \text{cm}^{-1}$. (d) The adaptive mesh generated for the inverse problem solution, with 418 nodes. Background $\mu_a = 0.050\ \text{cm}^{-1}$.

Table 2. The mesh scenarios and the background μ_a values in simulation study 1.

Mesh (forward)	Mesh (inverse)	Background μ_a (cm^{-1})
Uniform	Uniform	0.032, 0.036, 0.040, 0.044, 0.050
Adaptive	Uniform	0.032, 0.036, 0.040, 0.044, 0.050
Adaptive	Adaptive	0.032, 0.036, 0.040, 0.044, 0.050

For the inverse problem, we set the regularization parameter λ to 10^{-7} in all experiments to eliminate the dependence of the error estimates (2.15)–(2.19) on the regularization parameter. We consider the image reconstructed by using fine uniform meshes (61×61 nodes for the forward problem and 61×61 nodes for the inverse problem) as the reference image α^λ, which is assumed to possess no error due to discretization. We compute the error $\left\|\alpha^\lambda - \tilde{\alpha}_n^\lambda\right\|_{L^1(\Omega)}$ for each image reconstruction and tabulate the results in table 3. We see that the error in the images reconstructed by using uniform meshes for both forward and inverse problems is significantly reduced by the use of adaptively refined meshes. A similar behaviour is observed for all choices of background absorption value.

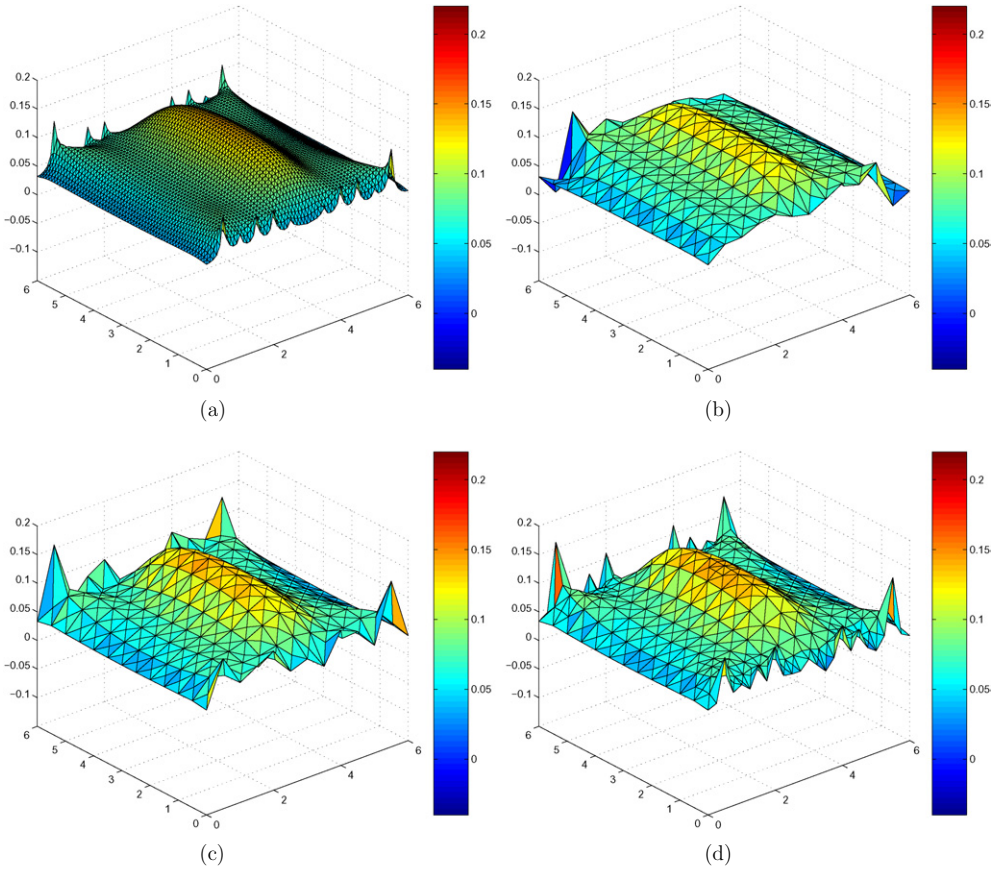

Figure 3. The reconstruction results of simulation study 1, with the background $\mu_a = 0.032\,\mathrm{cm}^{-1}$. (a) The optical absorption image used as the reference for error computations. (b) The reconstructed absorption image using the uniform mesh in figure 2(a) for the forward, and the uniform mesh in figure 2(b) for the inverse problem. (c) The reconstructed absorption image using an adaptive mesh for the forward, and the uniform mesh in figure 2(b) for the inverse problem. (d) The reconstructed absorption image using an adaptive mesh for the forward, and the adaptive mesh in figure 2(d) for the inverse problem.

Table 3. The error $\|\alpha^\lambda - \tilde{\alpha}_n^\lambda\|_{L^1(\Omega)}$ for each experiment described in the simulation study 1 and table 2. The first column shows the type of the meshes used in the forward and inverse problems, respectively. The unit of background μ_a is cm^{-1}.

	Background μ_a:	0.032	0.036	0.040	0.044	0.050
Uniform–uniform	$\|\alpha^\lambda - \tilde{\alpha}_n^\lambda\|_{L^1(\Omega)}$:	0.2325	0.2559	0.2773	0.2932	0.3013
Adaptive–uniform	$\|\alpha^\lambda - \tilde{\alpha}_n^\lambda\|_{L^1(\Omega)}$:	0.1238	0.1139	0.1166	0.1209	0.1278
Adaptive–adaptive	$\|\alpha^\lambda - \tilde{\alpha}_n^\lambda\|_{L^1(\Omega)}$:	0.1043	0.0997	0.0998	0.1003	0.1009

We present image reconstructions in figures 3 and 4 for the two extreme cases, where the background absorption value is equal to 0.032 and 0.050 cm^{-1}, respectively. Figures 3(a) and 4(a) display the reference images used to compute the error values given in table 3.

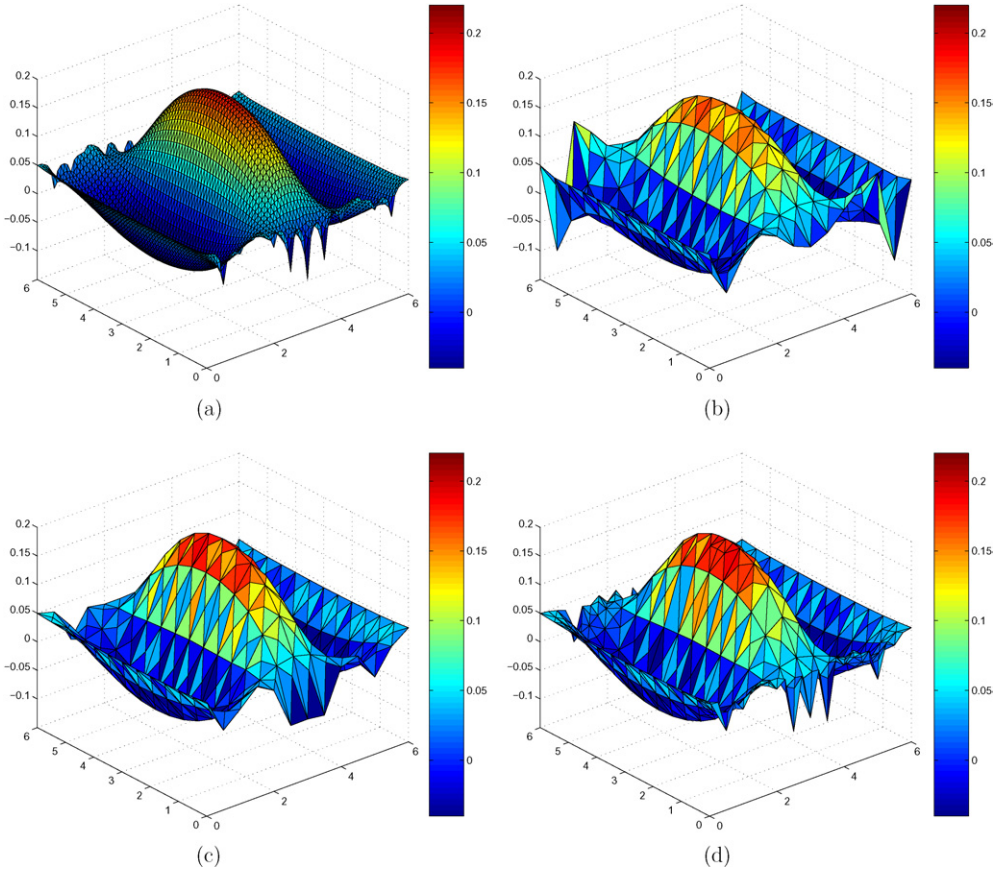

Figure 4. The results of simulation study 1, with the background $\mu_a = 0.050\ \text{cm}^{-1}$. (a) The optical absorption image used as the reference for error computations. (b) The reconstructed absorption image using the uniform mesh in figure 2(a) for the forward, and the uniform mesh in figure 2(b) for the inverse problem. (c) The reconstructed absorption image using an adaptive mesh for the forward, and the uniform mesh in figure 2(b) for the inverse problem. (d) The reconstructed absorption image using an adaptive mesh for the forward, and the adaptive mesh in figure 2(d) for the inverse problem.

Figures 3(c) and (d) show that the optical heterogeneity is resolved better by using adaptive meshes as compared to the reconstructed image obtained by using uniform meshes, which is shown in figure 3(b). These results are consistent with the error values given in table 3. A similar trend is seen in figures 4(c) and (d). Note that the number of nodes in the adaptive meshes is almost equal to the number of nodes that the uniform meshes have. In figure 5, we show the cross-sectional views from the reconstructed images. We see that the use of coarse uniform meshes fails to resolve the circular heterogeneity especially for the case in which the background $\mu_a = 0.032\ \text{cm}^{-1}$.

4.2. Simulation study 2

In this study, we consider the geometry shown in figure 1(b). To simulate the optical data, we use the same source–detector configuration considered in the first simulation study. We

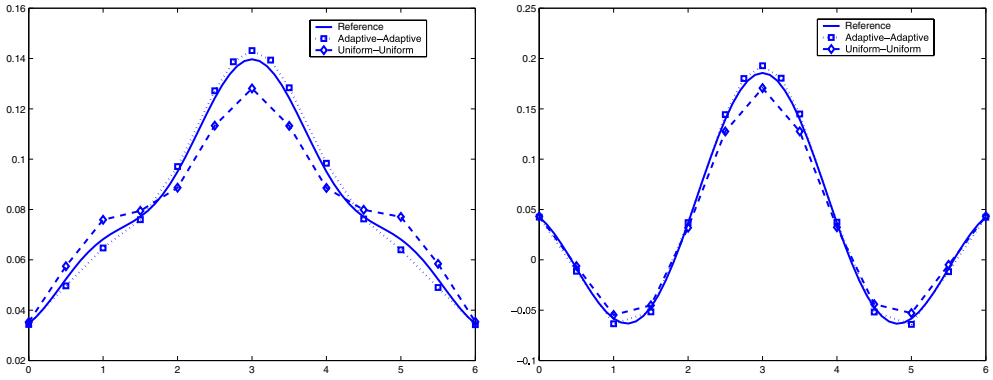

(a) (b)

Figure 5. The cross-sectional views from the reconstructed images in simulation study 1, corresponding to the cases where the background $\mu_a = 0.032$ and $\mu_a = 0.050\ \text{cm}^{-1}$, respectively. (a) The cross-sectional cuts taken from figures 3(a), (b) and (d), along the x-direction at $y = 3$. The solid, square and diamond lines correspond to the cross-sectional cuts taken from the images shown in figures 3(a), (b) and (d), respectively. (b) The cross-sectional cuts taken from figures 4(a), (b) and (d), along the x-direction at $y = 3$. The solid, square and diamond lines correspond to the cross-sectional cuts taken from the images shown in figures 4(a), (b) and (d), respectively.

simulate the optical data by solving the diffusion equation at $\omega = 0$ on a fine uniform grid with 81 nodes along the x and y directions, where the refractive index mismatch parameter $a = 3$. The diffusion coefficient D is assumed to be constant and $D(\mathbf{x}) = 0.0410$ cm, for all $\mathbf{x} \in \Omega \cup \partial\Omega$.

We consider four different radii for the circular heterogeneity with $\mu_a = 0.20\ \text{cm}^{-1}$ embedded in a background with $\mu_a = 0.040\ \text{cm}^{-1}$ as shown in figure 1(b). For each case, we compute the error for different mesh scenarios, similar to the first simulation study: uniform mesh for both forward and inverse problems; adaptive mesh for the forward problem and uniform mesh for the inverse problem; and adaptive meshes for both forward and inverse problems. The adaptive meshes for this simulation study were generated based on theorems 1 and 2, and the mesh generation algorithms described in the first simulation study and section 3. The uniform meshes used for the forward and inverse problems are identical to those used in the first simulation study. We note that the number of nodes in the adaptive meshes generated for the forward and inverse problems is close to the number of nodes in the corresponding uniform meshes.

In table 4, we tabulate the error norm $\left\|\alpha^{\lambda} - \tilde{\alpha}_n^{\lambda}\right\|$ obtained for each heterogeneity size with different mesh choices, where α^{λ} is the reference image reconstructed by using fine uniform meshes as in the first study. Table 4 shows that the error increases with increasing heterogeneity size. We see that the reduction in the error as a result of using adaptive meshes is more significant for smaller sized heterogeneities. Further reduction in the error norm $\left\|\alpha^{\lambda} - \tilde{\alpha}_n^{\lambda}\right\|$ is possible by increasing the number of nodes in the meshes.

For brevity, we only show the reconstruction results for the extreme cases: $r = 0.5$ cm and $r = 1.25$ cm. We note that the regularization parameter $\lambda = 5 \times 10^{-9}$ in all reconstructions. Figures 6(a) and (b) show the images used as the reference images α^{λ} in the calculation of the error norms $\left\|\alpha^{\lambda} - \tilde{\alpha}_n^{\lambda}\right\|$ listed in table 4. Figures 6(e)–(f) show that the adaptive meshes reduce the artefacts as compared to the images reconstructed by using uniform meshes, which are shown in figures 6(c)–(d).

Table 4. The L^1 norm of α^λ and the error $\|\alpha^\lambda - \tilde{\alpha}_n^\lambda\|_{L^1(\Omega)}$ for each experiment described in the simulation study 2. The first column shows the type of the meshes used in the forward and inverse problems, respectively. The radius of the circular heterogeneity is given in cm.

	Radius:	0.50	0.75	1.0	1.25
	$\|\alpha^\lambda\|_{L^1(\Omega)}$:	0.7196	1.3760	1.4759	1.7817
Uniform–uniform	$\|\alpha^\lambda - \tilde{\alpha}_n^\lambda\|_{L^1(\Omega)}$:	0.5622	0.5706	0.5850	0.6337
Adaptive–uniform	$\|\alpha^\lambda - \tilde{\alpha}_n^\lambda\|_{L^1(\Omega)}$:	0.2153	0.2776	0.3766	0.5113
Adaptive–adaptive	$\|\alpha^\lambda - \tilde{\alpha}_n^\lambda\|_{L^1(\Omega)}$:	0.2020	0.2630	0.3592	0.5034

4.3. Simulation study 3

In this simulation study, we consider the geometry shown in figure 1(c). The centre of the circular heterogeneity is moved vertically towards the detector side to see the effect on the imaging accuracy. Next, we show how the error in the reconstructed images due to discretization can be addressed by using appropriate meshes for the solutions of the forward and inverse problems. In this context, we compare the results obtained by using (1) uniform meshes, (2) the adaptive meshes generated using conventional *a priori* discretization error estimates, and (3) the adaptive meshes proposed in this study. By conventional error estimates, we mean the *a priori* discretization error estimates (2.16) and (2.17) for the solution of the forward problem, and the *a priori* interpolation error estimate (2.14) for the solution of the inverse problem.

To simulate the optical data, we use the same source–detector configuration considered in the first simulation study. We simulate the optical data by solving the diffusion equation at $\omega = 0$ on a fine uniform grid with 81 nodes along the x and y directions, where the refractive index mismatch parameter $a = 3$. We note that, in all reconstructions, the background absorption value is set to $\mu_a = 0.04$ cm^{-1} and the diffusion coefficient D is assumed to be constant and $D(\mathbf{x}) = 0.0410$ cm, for all $\mathbf{x} \in \Omega \cup \partial\Omega$.

The uniform meshes used in this simulation study are identical to those used in simulation studies 1 and 2. Sample meshes for the forward problem solution using the conventional and the proposed adaptive meshing strategies are shown in figures 7(a) and (b) and figures 8(c) and (d), respectively. We see that the conventional adaptive mesh generation strategy leads to meshes refined around only sources or detectors, but not both. In contrast, figures 8(c) and (d) show that the proposed strategy results in adaptive meshes refined around sources, detectors and the heterogeneity as well. This observation is consistent with theorem 2. The adaptive mesh for the inverse problem solution, which was generated using the *a priori* interpolation error estimate (2.14), is shown in figure 8(f). Note that the mesh was generated for the case where the circular heterogeneity was centred at (3.0, 3.5). The mesh generated based on theorem 1 (figure 8(e)) provides higher resolution close to the sources and detectors as compared to the mesh shown in figure 8(f), which is merely refined around the heterogeneity.

In this simulation study, we consider four different positions for the centre of the circular heterogeneity with radius 0.75 cm, along the y-axis: centre at (3.0, 3.0), (3.0, 3.5), (3.0, 4.0) and (3.0, 4.5), respectively. Similar to the previous simulations, we compute the error in the reconstructed images for all cases, and compare the error values attained by different meshing strategies. Finally we present the reconstructed images obtained by using different mesh strategies corresponding to the case where the circular inclusion is centred at (3.0, 3.5) and (3.0, 4.0).

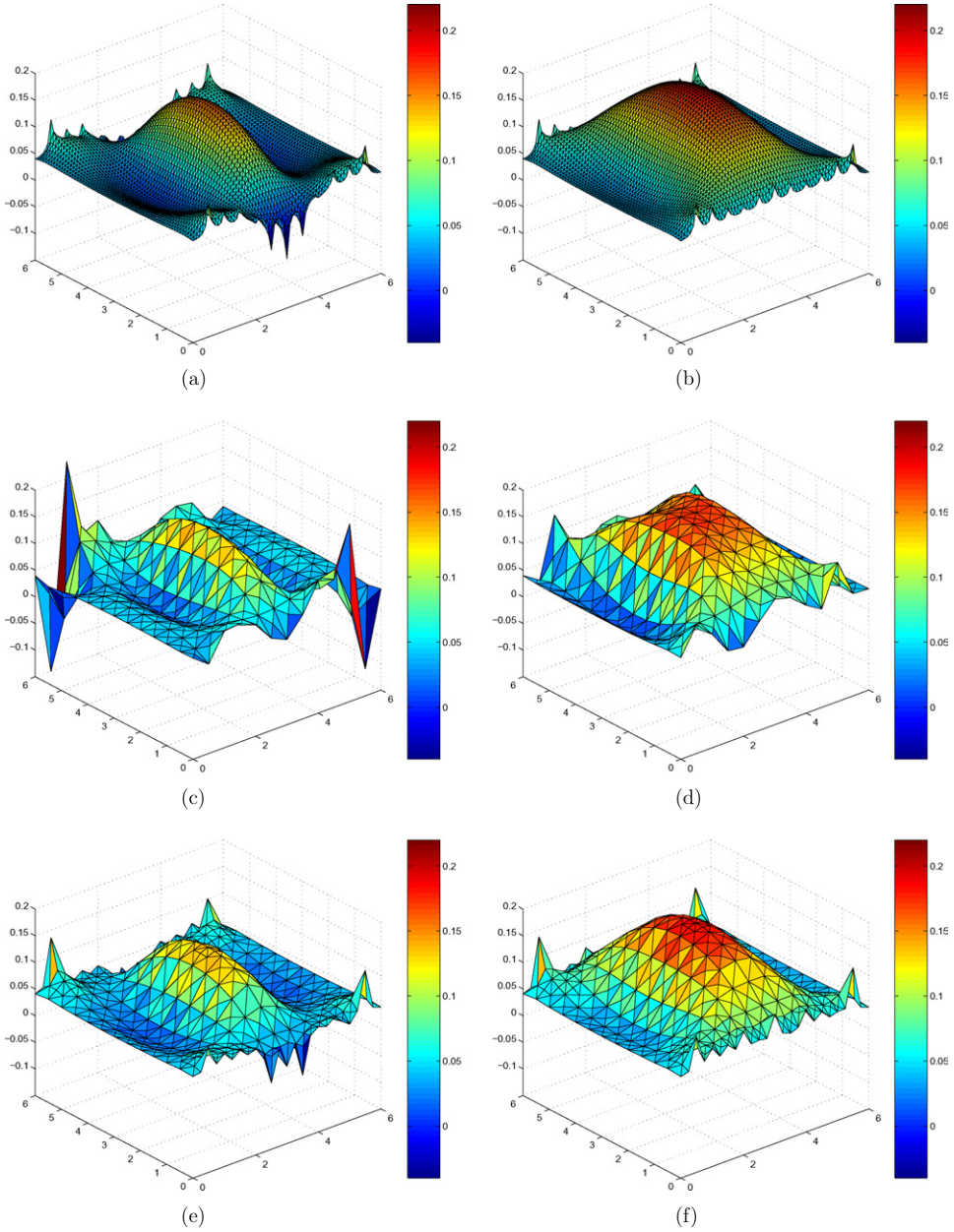

Figure 6. The results of simulation study 2. The left and right columns show the reconstructed images regarding the optical heterogeneity with radius 0.50 cm and 1.25 cm, respectively. The background $\mu_a = 0.040$ cm^{-1} in all of the reconstructions. The reference images shown in (a) and (b) are obtained using a uniform mesh with 61×61 nodes in both the forward and inverse problems. ((a) and (b)) The optical absorption images used as the reference for error computations. The images correspond to the reconstruction of the circular heterogeneities of radii 0.5 cm and 1.25 cm, respectively. ((c) and (d)) The reconstructed absorption images using the uniform mesh in figure 2(a) for the forward, and the uniform mesh in figure 2(b) for the inverse problem. ((e) and (f)) The reconstructed absorption image using adaptive meshes for both the forward and the inverse problems.

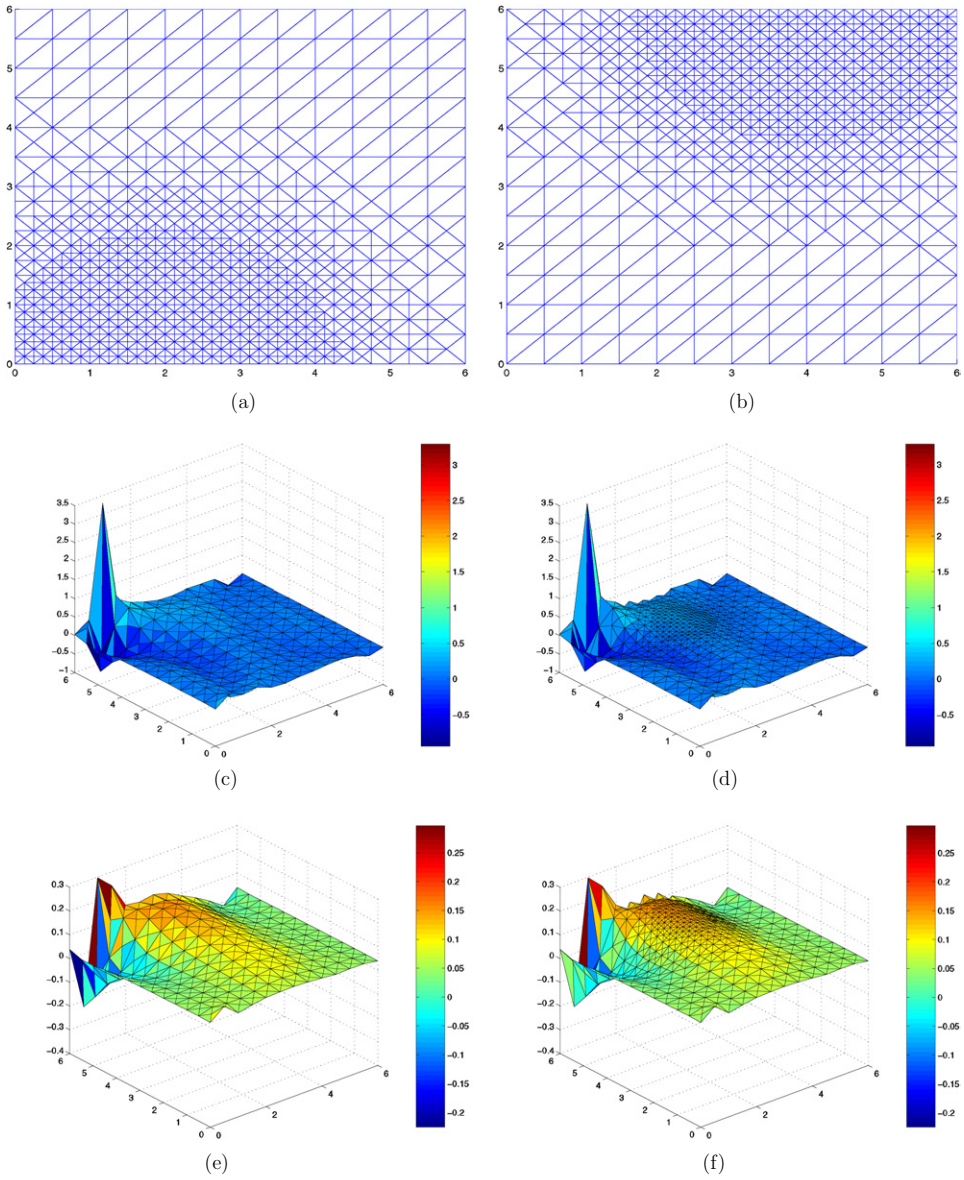

Figure 7. ((a) and (b)) Samples of adaptive meshes in the third simulation study (with 865 nodes for the source and the detector located at (2.0, 0) and (4.0, 6.0), respectively), generated by using the conventional error estimates (2.16) and (2.17), which led to unstable optical image reconstruction shown in (c) to (f), for the circular heterogeneity centred at (3.0, 3.5). ((c) and (d)) The unstable optical image reconstructions in the third simulation study, obtained by using the adaptive meshes for the forward problem solution whose examples are shown in (a) and (b) ($\lambda = 10^{-8}$). ((e) and (f)) The unstable optical image reconstructions in the third simulation study, obtained by using the adaptive meshes for the forward problem solution whose examples are shown in (a) and (b). λ was set to 10^{-6} to suppress the significantly large artefacts observed in (c) and (d).

Using the meshes for the forward problem discretization (see figures 7(a) and (b)), which were generated by using the conventional *a priori* discretization error estimates (2.16)–(2.17), leads to the image reconstructions shown in figures 7(c) and (d), where the

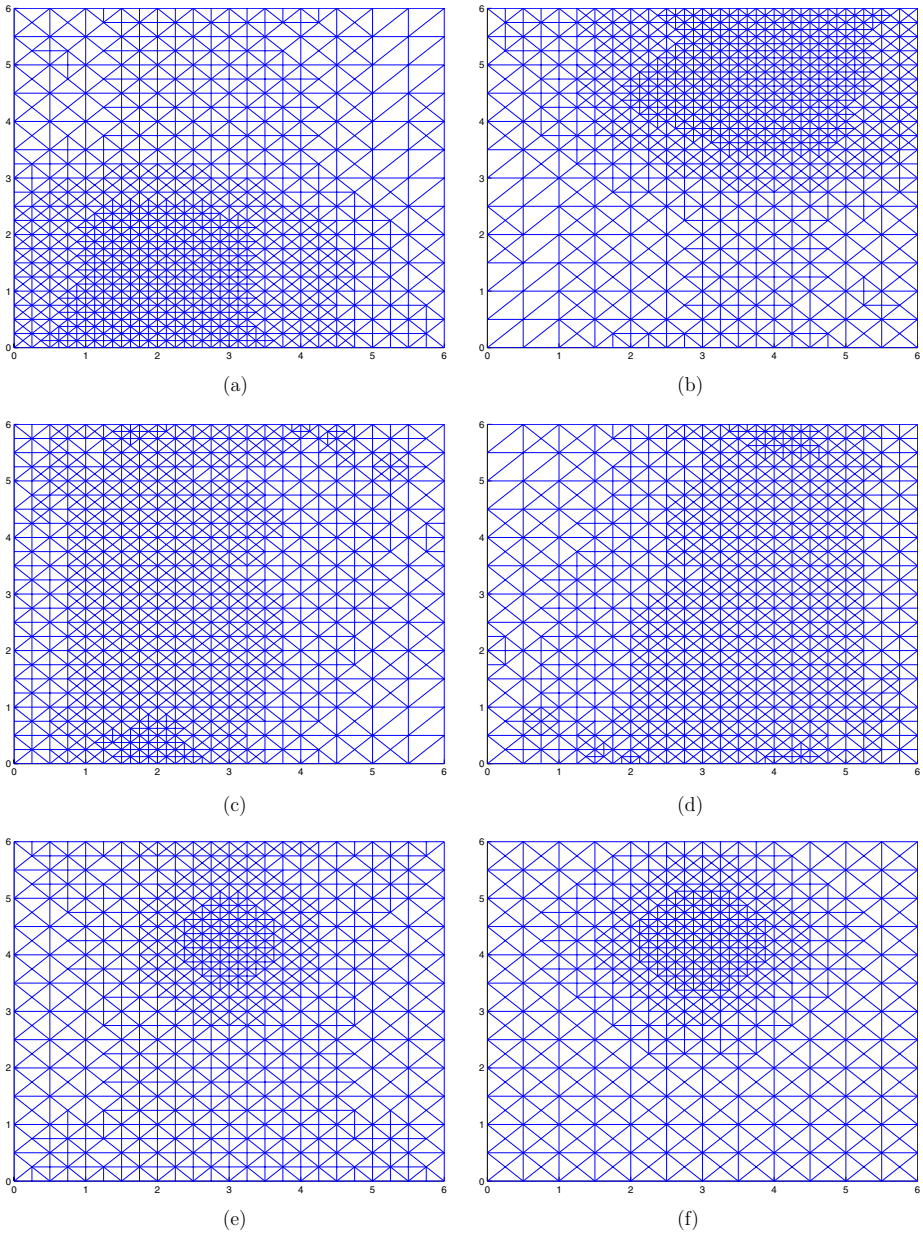

Figure 8. Samples of adaptive meshes used in the third simulation study, which led to the optical image reconstructions shown in figure 10. The meshes were generated for the circular heterogeneity centred at (3.0, 4.0). (a) The adaptive mesh with 942 nodes for the forward problem solution for the source located at (2.0, 0), obtained by refining the adaptive mesh shown in figure 7(a) around the detectors. (b) The adaptive mesh with 955 nodes for the forward problem solution for the detector located at (4.0, 6.0), obtained by refining the adaptive mesh shown in figure 7(b) around the sources. (c) The adaptive mesh with 895 nodes for the forward problem solution for the source located at (2.0, 0), generated based on theorem 2. (d) The adaptive mesh with 896 nodes for the forward problem solution for the detector located at (4.0, 6.0), generated based on theorem 2. (e) The adaptive mesh with 691 nodes for the inverse problem solution, generated based on theorem 1. (f) The adaptive mesh with 609 nodes for the inverse problem solution, generated based on the conventional error estimate (2.14).

regularization parameter $\lambda = 10^{-8}$. We observe that the finite-dimensional operator does not provide a stable solution. We note that using an adaptive mesh for the inverse problem solution does not change the outcome (figure 7(d)). Note also that the meshes generated by using the conventional *a priori* discretization error estimates (2.16)–(2.17) are sufficient to provide accurate finite element approximations to the actual solutions g_j and g_i^*. Therefore, the unstable reconstructions can be attributed to the errors $\mathcal{K}-\tilde{\mathcal{K}}$ and $\gamma-\tilde{\gamma}$, due to inappropriate discretization as noted by theorem 2. In consistence with theorem 2, this observation suggests that solving the forward problem accurately does not necessarily imply that approximate operator $\tilde{\mathcal{K}}$ and $\tilde{\gamma}$ are error-free. Therefore, in order to address such problems, one has to follow a discretization scheme based on theorem 2 for the solution of the forward problem, which takes into account the interaction between the solutions of the diffusion equation and the associated adjoint problem, as described in section 3.1.

In order to suppress the severe artefacts observed in figures 7(c) and (d), we increased the regularization parameter and set $\lambda = 10^{-6}$. The resulting images are shown in figures 7(e) and (f). As noted by theorems 1 and 2, increasing the regularization parameter reduces the error in the reconstructed images. However, increasing the regularization parameter will also compromise the image quality and lead to over-smoothed images. In order to address the instability issue without degrading the image quality by using high regularization parameters, we modified the adaptive mesh generation method that leads to the meshes shown in figures 7(a) and (b). In this context, for the first 2 refinements, we used the proposed mesh generation algorithm based on theorem 2 to generate an initial adaptive mesh; and for the next two refinements, we used the conventional error estimates (2.16)–(2.17). Following this modification, the samples of the resulting adaptive meshes are shown in figures 8(a) and (b). For a comparison, we also present in figures 8(c) and (d), the adaptive meshes generated by using the proposed adaptive mesh generation algorithms as described in section 3.1 and remark 1(iii). We observe that the meshes shown in figures 8(c) and (d), indicate further refinement around sources, detectors and the circular heterogeneity as compared to the adaptive meshes shown in figures 8(a) and (b).

Examples of the adaptive meshes generated for the inverse problem based on theorem 1 and the conventional *a priori* interpolation estimate (2.14) are shown in figures 8(e) and (f), respectively. We observe that the adaptive mesh shown in figure 8(e) provides higher resolution around sources and detectors as compared to the adaptive mesh shown in figure 8(f).

We note that the uniform meshes used in this simulation study are identical to those used in the previous simulation studies.

In order to compare the performance of the conventional and proposed adaptive mesh strategies, we perform four experiments and compute the error in the reconstructed optical absorption images. For each experiment, we consider five different mesh strategies and refer to table 5 for the description of these experiments.

We show the reconstructed optical absorption images for the two cases in figures 9 and 10, corresponding to the circular heterogeneity centred at (3.0, 3.5) and (3.0, 4.0), respectively. Figures 9(a) and 10(a) show the reference absorption image reconstructions which are used to compute the error in the reconstructed optical images.

Figure 9(b) shows the image reconstructed using coarse uniform meshes for both the forward and inverse problems, for the case where the circular inclusion is centred at (3.0, 3.5) where the regularization parameter was set to $\lambda = 10^{-8}$. With the same value of the regularization parameter, figure 9(c) shows the reconstructed image by using the adaptive mesh based on theorem 2 for the forward problem and the coarse uniform mesh (shown in figure 2(b)) for the inverse problem. Figure 9(e) shows the reconstructed image obtained

Table 5. The relevant parameters in experiments 1–5 in simulation study 3. The abbreviation 'Conv.' implies that the corresponding mesh was generated using the conventional *a priori* discretization error estimates (2.16)–(2.17) for the forward problem solution, and the conventional *a priori* interpolation error estimate (2.14) for the inverse problem solution. The abbreviation 'Prop.' refers to the adaptive meshes generated by using the proposed adaptive mesh generation algorithms based on theorems 1 and 2, for the inverse and forward problem solutions, respectively. The last column in the table shows the coordinates of the centre of the circular heterogeneity, considered in each experiment.

	Mesh (forward)	Mesh (inverse)	Centre at:
Exp. 1	Uniform	Uniform	[(3.0, 3.0), (3.0, 3.5), (3.0, 4.0), (3.0, 4.5)]
Exp. 2	Adaptive (Conv.)	Uniform	[(3.0, 3.0), (3.0, 3.5), (3.0, 4.0), (3.0, 4.5)]
Exp. 3	Adaptive (Conv.)	Adaptive (Conv.)	[(3.0, 3.0), (3.0, 3.5), (3.0, 4.0), (3.0, 4.5)]
Exp. 4	Adaptive (Prop.)	Uniform	[(3.0, 3.0), (3.0, 3.5), (3.0, 4.0), (3.0, 4.5)]
Exp. 5	Adaptive (Prop.)	Adaptive (Prop.)	[(3.0, 3.0), (3.0, 3.5), (3.0, 4.0), (3.0, 4.5)]

Table 6. The error $\|\alpha^{\lambda} - \tilde{\alpha}_n^{\lambda}\|_{L^1(\Omega)}$ for each experiment described in the simulation study 3. The first column shows the type of the meshes used in the forward and inverse problems, respectively. The superscript 'C' denotes that the corresponding adaptive mesh generation is based on the conventional *a priori* error estimates (2.16)–(2.17) and (2.14).

	Radius at:	(3.0, 3.0)	(3.0, 3.5)	(3.0, 4.0)	(3.0, 4.5)
Uniform–uniform	$\|\alpha^{\lambda} - \tilde{\alpha}_n^{\lambda}\|_{L^1(\Omega)}$:	0.4539	0.4606	0.4733	0.4956
Adaptive–uniform	$\|\alpha^{\lambda} - \tilde{\alpha}_n^{\lambda}\|_{L^1(\Omega)}$:	0.2690	0.2695	0.2634	0.2507
Adaptive–adaptive	$\|\alpha^{\lambda} - \tilde{\alpha}_n^{\lambda}\|_{L^1(\Omega)}$:	0.2433	0.2455	0.2459	0.2434
Adaptive–uniform	$\|\alpha^{\lambda} - \tilde{\alpha}_n^{\lambda,C}\|_{L^1(\Omega)}$:	0.7989	0.7596	0.7072	0.6418
Adaptive–adaptive	$\|\alpha^{\lambda} - \tilde{\alpha}_n^{\lambda,C}\|_{L^1(\Omega)}$:	0.8011	0.7614	0.7070	0.6351

by using the adaptive meshes based on theorems 1 and 2. We observe the improvements especially around the boundaries. Using the conventional adaptive meshes for the forward problem solution, which were modified around sources and detectors as noted before, we ran into a similar instability problem. Therefore, in order to obtain better reconstructions with the conventional adaptive meshes, we set the regularization parameter $\lambda = 10^{-7}$ in the corresponding inverse problem formulations. The resulting reconstructed images are shown in figures 9(c) and (f). In this case, we observe that the use of conventional adaptive meshes for the forward and inverse problems does not improve the image quality as compared to the reconstructed image shown in figure 9(b), which is obtained by using coarse uniform meshes.

We observe similar results for the case where the circular inclusion is centred at (3.0, 4.0). We note that the regularization parameter is set to $\lambda = 10^{-8}$ for all reconstructions except for the reconstructions obtained by using conventional adaptive meshes, in which case $\lambda = 10^{-7}$. Figure 9 shows the reconstructed images corresponding to all meshing strategies.

Table 6 shows the error norm $\alpha^{\lambda} - \tilde{\alpha}_n^{\lambda}$ computations for all cases. Similar to the previous experiments, α^{λ} is the reference image obtained by using fine uniform meshes for the discretization of the forward and inverse problems. The error values are consistent with figures 9 and 10. In all cases, the proposed adaptive meshes significantly reduce the error in the reconstructed images. Furthermore, the image quality is enhanced by merely appropriate discretization, without having to increase the regularization parameter. In contrast, the conventional adaptive meshes perform worse than uniform meshes even though a higher regularization parameter is used.

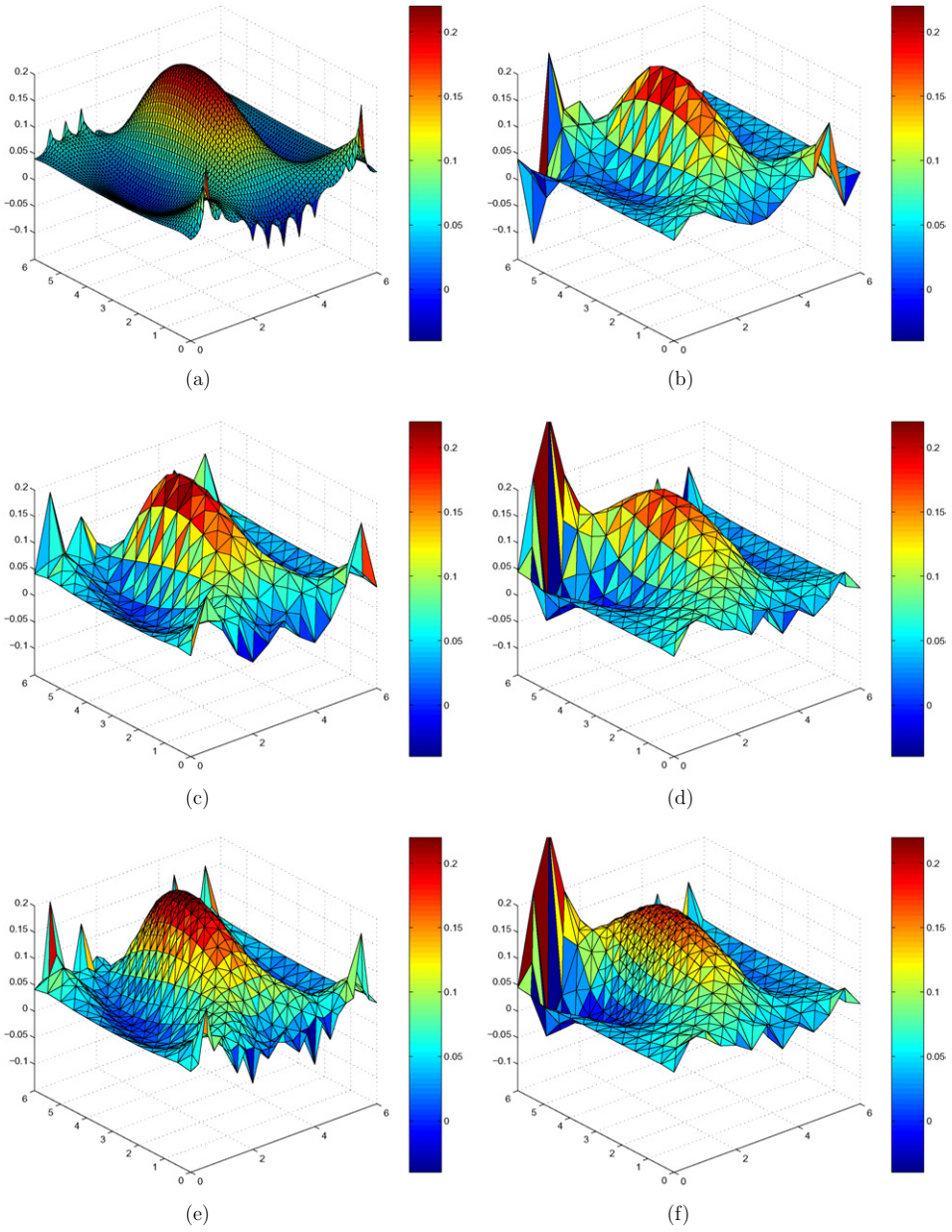

Figure 9. The reconstructed optical images regarding the circular heterogeneity centred at (3.0, 3.5) in the third simulation study. (a) The absorption image used as the reference in the error computations. (b) The reconstructed absorption image using the uniform mesh in figure 2(a) for the forward, and the uniform mesh in figure 2(b) for the inverse problem. (c) The reconstructed absorption image using adaptive meshes based on theorem 2 for the forward, and the uniform mesh in figure 2(b) for the inverse problem. (d) The reconstructed absorption image using adaptive meshes based on *a priori* error estimates (2.16) and (2.17) for the forward, and the uniform mesh in figure 2(b) for the inverse problem. (e) The reconstructed absorption image using adaptive meshes based on theorem 2 for the forward, and using the adaptive mesh based on theorem 1 for the inverse problem. (f) The reconstructed absorption image using adaptive meshes based on *a priori* error estimates (2.16) and (2.17) for the forward, and the interpolation error estimate (2.14) for the inverse problem.

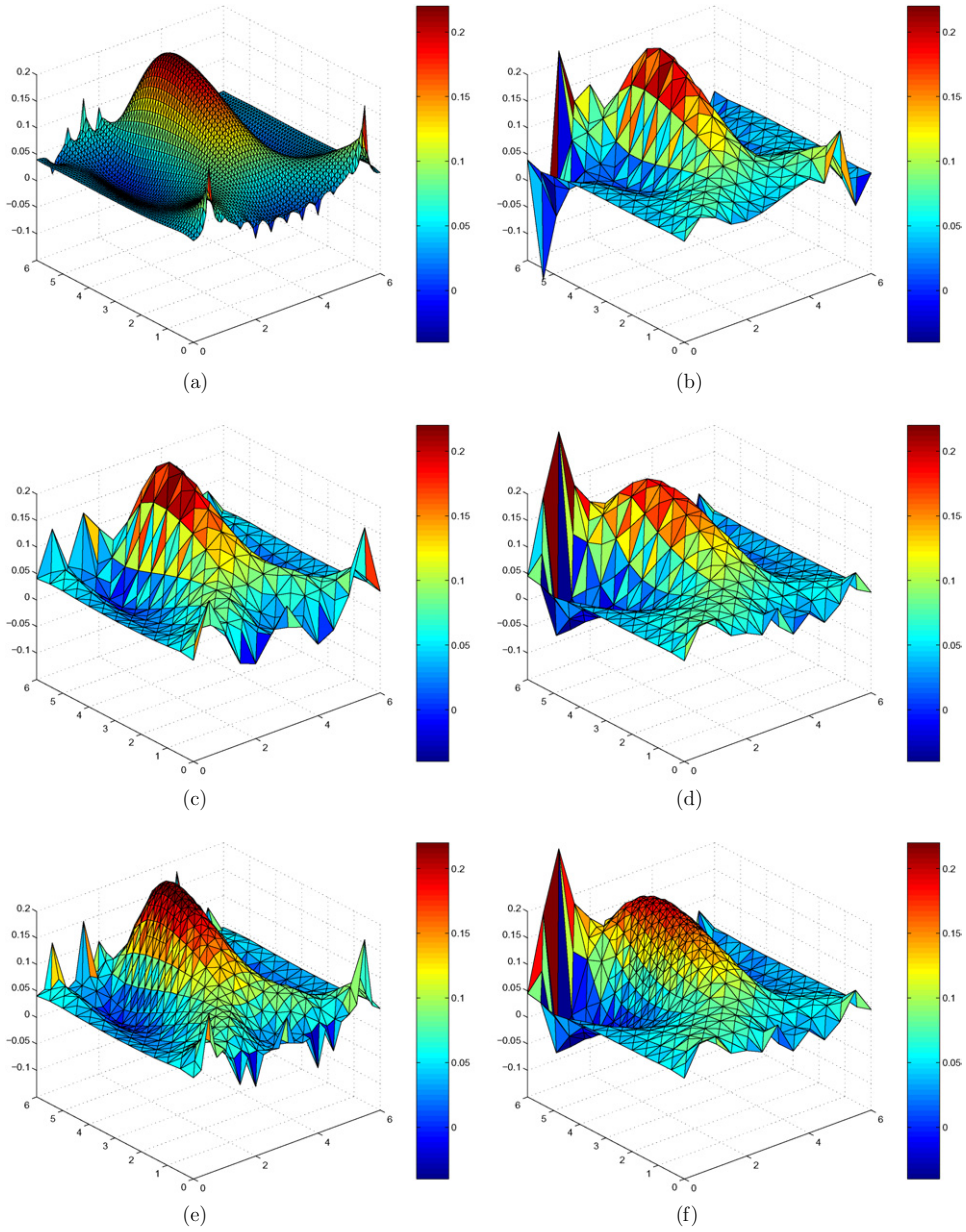

Figure 10. The reconstructed optical images regarding the circular heterogeneity centred at (3.0, 4.0) in the third simulation study. (a) The absorption image used as the reference in the error computations. (b) The reconstructed absorption image using the uniform mesh in figure 2(a) for the forward, and the uniform mesh in figure 2(b) for the inverse problem. (c) The reconstructed absorption image using adaptive meshes based on theorem 2 for the forward, and the uniform mesh in figure 2(b) for the inverse problem. (d) The reconstructed absorption image using adaptive meshes based on *a priori* error estimates (2.16) and (2.17) for the forward, and the uniform mesh in figure 2(b) for the inverse problem. (e) The reconstructed absorption image using adaptive meshes based on theorem 2 for the forward, and the adaptive mesh based on theorem 1 for the inverse problem. (f) The reconstructed absorption image using adaptive meshes based on *a priori* error estimates (2.16) and (2.17) for the forward, and the interpolation error estimate (2.14) for the inverse problem.

5. Conclusion

In this work, based on the error analysis presented in part I [9], we developed two new adaptive mesh generation algorithms, one for the forward and one for the inverse problem, which take into account the interdependence between the solutions of the two problems. We have also presented the computational complexity of the presented adaptive mesh generation algorithms. Our numerical experiments provided a verification of theorems 1 and 2 and showed that the proposed mesh generation algorithms significantly improve the accuracy of the reconstructed optical images for a given number of unknowns in the discrete forward and inverse problems. Conventional error estimates do not include domain-specific factors. As a result, the adaptive mesh generation algorithms based on conventional error estimates (2.16)–(2.17) and (2.14) may lead to high errors in reconstructed optical images as demonstrated in our numerical experiments.

We finally note that the adaptive mesh generation algorithms introduced in this paper can be adapted for the forward and inverse problems of similar inverse parameter estimation problems, such as electrical impedance tomography, optical fluorescence tomography, bioluminescence tomography, microwave imaging etc.

Acknowledgments

This material is based upon work supported by NSF-BES-0353160, ONR-N00014-04-1-0694 and US Army Medical Research-W81XWH-04-1-0559. Any opinions, findings and conclusions or recommendations expressed in this material are those of the authors and do not necessarily reflect the views of the National Science Foundation. Various portions of this research were supported by the Center for Subsurface Sensing and Imaging Systems, under the Engineering Research Centers Program of the National Science Foundation (Award Number EEC-9986821) and Rensselaer Polytechnic Institute.

Appendix. Solution of the model problem

In order to initialize the adaptive mesh for the solution of the forward problem (provided $D(\mathbf{x}) = \overline{D}$ and $\mu_a(\mathbf{x}) = \overline{\mu_a}$ are spatially constant), we use an analytical solution to compute the estimates of g_j and g_i^*. Below, we give the solution in 2D for (2.1). Under the same conditions, an analytical solution for the adjoint problem (2.3) can be obtained in a similar way.

First, we use the polar coordinates (ρ, θ) to rewrite (2.1):

$$\frac{1}{\rho}\frac{\partial}{\partial\rho}\left(\rho\frac{\partial g_j}{\partial\rho}\right) + \frac{1}{\rho}\frac{\partial}{\partial\theta}\left(\rho\frac{\partial g_j}{\partial\theta}\right) + K_\Omega^2 g_j = -\frac{4\pi}{\rho}\frac{\delta\left(\rho-\rho_s^j\right)\delta\left(\theta-\theta_s^j\right)}{\overline{D}},$$

where we consider an unbounded domain, model the point source located at $\left(\rho_s^j, \theta_s^j\right)$ by the Dirac-delta function $4\pi\delta\left(\rho-\rho_s^j\right)\delta\left(\theta-\theta_s^j\right)/\rho$ and $K_\Omega^2 = -(\overline{\mu_a}c+\mathrm{i}\omega)/c\overline{D}$. Then, the solution g_j at (ρ, θ) due to the point source located at $\left(\rho_s^j, \theta_s^j\right)$ is given by [11]

$$g_j\left(\rho, \rho_s^j; \theta, \theta_s^j\right) = \frac{4}{\overline{D}\pi}\left\{\frac{1}{2}I_0(k_\Omega\rho_<)K_0(k_\Omega\rho_>) + \sum_{m=1}^{\infty}\cos[m(\theta-\theta_s)]I_m(k_\Omega\rho_<)K_m(k_\Omega\rho_>)\right\},$$

where $\rho_<$ means the smaller of ρ and ρ_s^j, $\rho_>$ means the greater of ρ and ρ_s^j, I_m and K_m are the modified Bessel functions of the first and second kind, respectively [1] and $k_\Omega = \sqrt{-K_\Omega^2}$.

The solution of the problem in 3D can be derived in a similar manner [11, 17].

References

[1] Abramowitz M and Stegun I A 1968 *Handbook of Mathematical Functions* (New York: Dover)

[2] Arridge S R 1999 Optical tomography in medical imaging *Inverse Problems* **15** R41–93

[3] Arridge S R, Kaipio J P, Kolehmainen V, Schweiger M, Somersalo E, Tarvainen T and Vauhkonen M 2006 Approximation errors and model reduction with an application in optical diffusion tomography *Inverse Problems* **22** 175–95

[4] Brankov J G, Yang Y and Wernick M N 2004 Tomographic image reconstruction based on a content-adaptive mesh model *IEEE Trans. Med. Imaging* **23** 202–12

[5] Brenner S C and Scott L R 2002 *The Mathematical Theory of Finite Element Methods* (Berlin: Springer)

[6] Eppstein M J, Dougherty D E, Hawrysz D J and Sevick-Muraca E M 2001 Three-dimensional Bayesian optical image reconstruction with domain decomposition *IEEE Trans. Med. Imaging* **20** 147–63

[7] Gu X, Xu Y and Jiang H 2003 Mesh-based enhancement schemes in diffuse optical tomography *Med. Phys.* **30** 861–9

[8] Guven M, Yazici B, Intes X and Chance B 2003 An adaptive multigrid algorithm for region of interest diffuse optical tomography *Int. Conf. in Image Processing Proc. of IEEE* **2** 823–6

[9] Guven M, Yazici B, Kwon K, Giladi E and Intes X 2007 Effect of discretization error and adaptive mesh generation in diffuse optical absorption imaging: I *Inverse Problems* **23** 1115–33

[10] Huang M and Zhu Q 2004 Dual-mesh optical tomography reconstruction method with a depth correction that uses *a priori* ultrasound information *Appl. Opt.* **43** 1654–62

[11] Jackson J D 1962 *Classical Electrodynamics* (New York: Wiley)

[12] Joshi A, Bangerth W and Sevick-Muraca E M 2004 Adaptive finite element based tomography for fluorescence optical imaging in tissue *Opt. Exp.* **12** 5402–17

[13] Kress R 1999 Linear integral equations *Applied Mathematical Sciences* vol 82 2nd edn (Berlin: Springer)

[14] Molinari M, Cox S J, Blott B H and Daniell G J 2001 Adaptive mesh refinement techniques for electrical impedance tomography *Physiol. Meas.* **22** 91–6

[15] Rivara M C 1984 Mesh refinement processes based on the generalized bisection of simplices *SIAM J. Numer. Anal.* **21** 604–13

[16] Torregrossa M, Zint C V and Poulet P 2002 Image reconstruction in optical tomography: mesh influence *4th Int. Workshop: Computational Problems of Electrical Engineering* pp 183–6

[17] Walker S, Boas D A and Gratton E 1998 Photon density waves scattered from cylindrical inhomogeneities: theory and experiments *Appl. Opt.* **37** 1935–44